Neurogenesis and vascularization of the damaged brain using a lactate-releasing biomimetic scaffold

Zaida Álvarez [a,b,d], Oscar Castaño [a,c,d], Alba A. Castells [b], Miguel A. Mateos-Timoneda [a,d], Josep A. Planell [a], Elisabeth Engel [a,c,d], Soledad Alcántara [b,*]

[a] Institute for Bioengineering of Catalonia-IBEC, Barcelona, Spain
[b] Dpt. of Pathology and Experimental Therapeutics, Medical School (Bellvitge Campus), University of Barcelona-UB, Barcelona, Spain
[c] Dpt. Material Science and Metallurgical Engineering, Technical University of Catalonia-UPC, Barcelona, Spain
[d] CIBER en Bioingeniería, Biomateriales y Nanomedicina (CIBER-BBN), Barcelona, Spain

ARTICLE INFO

ABSTRACT

Regenerative medicine strategies to promote recovery following traumatic brain injuries are currently focused on the use of biomaterials as delivery systems for cells or bioactive molecules. This study shows that cell-free biomimetic scaffolds consisting of radially aligned electrospun poly-L/DL lactic acid (PLA70/30) nanofibers release L-lactate and reproduce the 3D organization and supportive function of radial glia embryonic neural stem cells. The topology of PLA nanofibers supports neuronal migration while L-lactate released during PLA degradation acts as an alternative fuel for neurons and is required for progenitor maintenance. Radial scaffolds implanted into cavities made in the postnatal mouse brain fostered complete implant vascularization, sustained neurogenesis, and allowed the long-term survival and integration of the newly generated neurons. Our results suggest that the endogenous central nervous system is capable of regeneration through the *in vivo* dedifferentiation induced by biophysical and metabolic cues, with no need for exogenous cells, growth factors, or genetic manipulation.

© 2014 Elsevier Ltd. All rights reserved.

1. Introduction

Stroke and traumatic injury are common causes of disability, with loss of nerve tissue due to secondary degeneration, gliosis, and often the formation of cavities that inhibit neural cell growth [1,2]. Unfortunately, the clinical efficacy of regenerative medicine strategies for nerve tissue regeneration has been limited by the poor effective integration, vascularization, and survival of the implants and the defective differentiation of exogenous neural stem cells (NSCs) [3–6]. Recent attempts at neural cell regeneration have therefore focused on the use of engineering materials that mimic the adult NSC niche, in order to establish an adequate environment for neurogenesis and differentiation. Biophysical cues and the release of biochemical factors are the principal parameters that regulate NSC survival and differentiation [4,7]. However, because

the adult mammalian NSC niche has limited regenerative capacities, effective regeneration of the central nervous system (CNS) requires the reconstitution of its embryonic counterpart [8–11]. During development, radial glia are the principal NSCs that generate neurons and glia. Radial glia span the entire CNS parenchyma and serve as substrates for neuronal migration [12–14]. During early neurogenesis, blood vessels invade the CNS and interact with NSCs, giving rise to the neurovascular niche [15,16]. In the adult brain, neurogenic radial glia can be regained, at least to some extent, after injury [17,18], indicating an endogenous attempt at reconstitution of the embryonic NSC niche.

The goal of this study was to design an implantable biomaterial scaffold that reproduces the 3D organization and supportive function of embryonic radial glia. Radial glia are bipolar cells with 1- to 2-μm-thick shafts that form a palisade [19]. They contain high levels of glycogen and release L-lactate [20], a common cellular cue that induces angiogenesis [21] and supports neuronal and NSC/progenitor metabolism [22]. Lactate is also a component of widely used biobased plastics made from poly-lactic-acid polymers. In a previous work we observed that poly(L-lactide-co-D,L-lactide)

* Corresponding author. Cell Biology Unit, Department of Experimental Pathology and Therapeutics, School of Medicine (Bellvitge Campus), University of Barcelona, 08907 L'Hospitalet de Llobregat, Barcelona, Spain. Tel./fax: +34 934024288.
E-mail address: salcantara@ub.edu (S. Alcántara).

(PLDLLA) 70/30 (70% pure L, and 30% DL) films were better *in vitro* substrates than PLDLLA 95/5 (95% pure L, and 5% DL) in terms of cortical neural cell growth and the maintenance of pools of neuronal and glial progenitor cells [23]. The difference between PLDLLA 70/30 and the usual PLLA (pure L isomer) is that in the former mismatching of the polymer chains promotes less order, less crystallinity, a higher degree of amorphicity, and therefore, a higher degradation rate. We also demonstrated the importance of controlling topography in order to dedifferentiate glial cells [24]. Thus, the biomimetic scaffold used in the present work combines the neurogenic and radial-glia-inducing properties of lactate-releasing PLDLLA 70/30 (PLA) with a topology that mimics their 3D organization of radial glia.

Here we show that L-lactate released by PLA nanofibers is required for NSC/progenitor maintenance. Radially aligned PLA nanofiber scaffolds implanted into cavities made in the postnatal mouse brain were observed to mimic some of the physical and biochemical characteristics of radial glia *in vivo*. This enabled robust and functional vascularization in the direction of fiber orientation, NSC niche activation, neurogenesis, and neuronal survival and integration into normal brain circuits for more than 1 year. Our results suggest the possibility of endogenous central nervous system regeneration through *in vivo* dedifferentiation induced by biophysical and metabolic cues, with no need for exogenous cells, growth factors, or genetic manipulation.

2. Materials and methods

2.1. PLA70/30 nanofiber characterization

Poly-L/DL lactic acid 70/30 (PLA70/30) (Purasorb PLDL 7038, inherent viscosity midpoint 3.8 DL/g, molecular mass ≈ 850,000 Da) was purchased from Purac Biomaterials (Gorinchem, The Netherlands). The 238 ± 18-μm-thick sheets of random and aligned PLA70/30 nanofibers were prepared by electrospinning. Briefly, 2.86 g (4% w/w) of PLA was dissolved in 50 ml of 2,2,2-trifluoroethanol (99.8%; Panreac, Barcelona, Spain). The solution was electrospun with a grounded flat collector for randomly distributed fiber samples or with a grounded rotary collector with a diameter of 9 cm and a rotational speed of 1000 rpm for aligned ones. The voltage was 8 kV, the distance between the tip and the collector was 12 cm, and the humidity was 20% at 23 °C.

PLA70/30 wettability was characterized by contact-angle measurements with an OCA 20 system (Dataphysics GmbH, Filderstadt, Germany), using the captive bubble technique. This method measures the equilibrium angle formed between a 3-ml air bubble and the PLA surface, both immersed in water. The measurements were performed in triplicate with at least three different data points for each sample.

The ζ-potential was measured using a SurPASS electrokinetic analyzer and VisioLab software (Anton Paar Ltd., Graz, Austria). All measurements were done at a dynamic pH of the electrolyte (1 mM KCl, pH 3–8) after 1 h of equilibration and using the adjustable gap cell for small samples.

The stiffness and surface topography of PLA70/30 nanofibers were measured by atomic force microscopy (AFM) (MultiMode 8 atomic force microscope; Bruker). Young's modulus and the tensile strength of the fibrous sheets were determined with a Zwick-Roell Zwicki-Line Z0.5TN (Zwick-Roell, Ulm, Germany) universal testing machine, with ten samples of 40 × 10 mm. The tensile stress test was monitored at a speed of 10 mm/min.

The two conformations of the PLA70/30 nanofibers were characterized by differential scanning calorimetry (DSC, Mettler DSC-822e calorimeter with a TS0801RO robotic arm). Samples of approximately 5 mg were placed in aluminum crucibles under a nitrogen atmosphere and heated from room temperature up to 180 °C at a rate of 10 °C/min. The degree of crystallinity was assessed by the following equation (1):

$$\%\chi_c = \frac{(\Delta H_m - \Delta H_c)}{\Delta H_m^0} \tag{1}$$

where $\%\chi_c$ is the percentage crystallinity, ΔH_m is the latent heat of melting, ΔH_c is the heat of the crystallization, and ΔH_m^0 is the melting heat of PLA with an assumed degree of crystallinity of 100% ($\Delta H_m^0 = 93.1$ J/g).

An X'Pert PRO diffractometer (Panalytical, Almelo, Netherlands) (CuKα $\lambda = 1.5406$ Å radiation, 45 kV, 40 mA, and a step size of 0.026°) was used in $\theta/2\theta$ 2–60° X-ray diffraction (XRD) analyses of PLA films.

Micro- and nano-morphologies were assessed using a field emission scanning electron microscope (Nova-Nano SEM-230; FEI Co., Netherlands), operating at 10 kV and with ultra-thin carbon coating of the fibers. The fiber sheets were cross-sectioned using the focused ion beam lithography technique (Strata DB235; FEI Co.).

2.2. Degradation study and L-lactate quantification

The degradation of PLA nanofibers *in vitro* was followed at 37 °C for eight weeks. Four samples were immersed in glucose- and pyruvate-free Neurobasal A (NB-A; Gibco) and retrieved after 5, 7, 21, 30, and 45 days *in vitro* (div). The L-lactate concentration was determined as previously described [23].

2.3. Cell culture

All animal housing and procedures were approved by our institution's Animal Care and Use Committee, in accordance with Spanish and EU regulations. Glial cells were derived from the cerebral cortex of newborn mice (P0) as previously described [24]. The influence of the properties of the various materials used in this study on glial cell adhesion, morphology and differentiation was determined as follows: passage 1 (Ps1) cells were cultured at a density of 2×10^5 cells/cm^2 for 5 div in NB containing 3% normal human serum (NHS), 1% penicillin–streptomycin (pen–strep), and 2 mM L-glutamine on uncoated PLA70/30 nanofibers. Control Ps1 glial cells were cultured on non-coated culture plastic (for western blotting) or on glass coverslips (for immunocytochemistry) under the same conditions used for PLA nanofibers. Both the cell composition and the biochemical characterization of control and reference glial conditions were described previously [24].

Neurons were obtained from embryonic brains as described elsewhere [23]. The cells were plated at a density of 2.5×10^5 cells/cm^2 directly, either on top of random and aligned nanofibers or, as a positive control, on poly-D-lysine (Sigma–Aldrich) coated tissue culture plates (for western blotting) or glass coverslips (for immunocytochemistry) for 5 div. In co-cultures, embryonic-day 16 (E16) neurons were plated at a density of 2.5×10^5 cells/cm^2 directly on top of 5-div glial cell cultures and then cultured for 5 more days in serum-free NB supplemented with 1% pen-strep, 0.5 mM L-glutamine, 1× B27 (Gibco), 5.8 μl/ml 7.5% NaHCO$_3$ (neuronal medium). To analyze the effect of lactate, E16 neurons were cultured on aligned PLA70/30 nanofibers in glucose-containing NB or in glucose-free NBA supplemented with 1% NHS, 1% pen-strep, 0.5 mM L-glutamine, 22 mM glutamic acid, 1× B27, and 5.8 μl 7.5% NaHCO$_3$/ml for 24 h, after which the medium was replaced with serum-free neuronal medium in the presence or absence of 100 nM of the monocarboxylate transporter (MCT) 1/2 inhibitor AR-C155858 (AdooQ, Irvine, CA, USA) for four more days. The samples were either fixed in 4% paraformaldehyde for immunocytochemistry or used for protein extraction and western blot analysis.

2.4. Video time-lapse microscopy

For video time-lapse analysis, neurons were obtained from the cerebral cortex of E16 mice and cultured at low density on top of aligned PLA nanofibers. After 5 div, the cells were placed in the incubation chamber of an Observer Z1m inverted fluorescence microscope (Carl Zeiss, USA) at 37 °C with 5% CO$_2$ and observed by phase-contrast microscopy. Images were obtained every minute for 15 h. Cell displacement, speed, and trajectory were calculated using the "Manual Tracking" plug-in of the ImageJ software (National Institutes of Health, USA).

2.5. Implantation of PLA nanofiber tubes into the right hemisphere of the injured mouse brain

Four-day-old (P4) mice were anesthetized by immersion in ice for 5 min, placed in a stereotaxic apparatus for small animals (Stoelting Europe, Dublin, Ireland mouse and neonatal rat stereotaxic adaptor), and kept cold during surgery. A triangular tissue flap overlying the right somatosensory cortex was lifted with a surgical blade, carefully avoiding severing surface blood vessels in the brain parenchyma. After opening the skull, 1-mm^3 cavities were made by direct suction with a syringe connected to a blunt needle (1 mm ø). Immediately after tissue removal, 1-mm^3 nanofiber tubes were soaked in NB containing 1% pen–strep and implanted into the cavity ($n = 96$). As a control, the cavity was left empty and the tissue flap put back in place. The mice were then warmed on a heating pad and returned to their mother after recovery. The two groups of mice were killed at 2 or 7 days or at 2, 6, 12, or 15 months following implantation, and the brains were processed for immunocytochemistry as described above.

2.6. Immunofluorescence of cultured cells and western blot analysis

Total protein extracts for western blot analysis were prepared from primary neuronal and glial cultures, separated by SDS-polyacrylamide gel electrophoresis, and electro-transferred to a nitrocellulose membrane (Bio-Rad). The membranes were blocked with 5% bovine serum albumin (BSA, Sigma–Aldrich) and incubated overnight at 4 °C first with primary antibodies and then with the corresponding secondary HRP-conjugated antibodies (1:3000; Santa Cruz Biotechnology). Protein signals were detected by the ECL chemiluminescent system (Amersham, GE Healthcare). Densitometry analysis, standardized to actin as a control for protein loading, was carried out with ImageJ software (National Institutes of Health, USA). For quantification, triplicate samples were analyzed and at least three different experiments were performed.

For immunofluorescence, fixed primary cultures or tissue sections were incubated with primary antibodies overnight at 4 °C and then with the appropriate Alexa 488 or Alexa 555 secondary antibodies (1:500, Molecular Probes). To-Pro-3 iodide (TOPRO-3, 1:500, Molecular Probes) was used to stain nuclei. Finally, the preparations were cover-slipped with Mowiol (Calbiochem) for imaging.

2.7. Detection and characterization of neural populations

The mice were perfused with 4% paraformaldehyde and their brains were removed and cryosectioned coronally at 40-μm intervals. To characterize the phenotype of the cells inside the scaffold, the following primary antibodies were used: mouse anti-NeuN (neuronal marker, 1:500; Abnova Corp., Taipei, Taiwan), rabbit anti-parvalbumin (PV, gabaergic neuronal marker, 1:8000; Swant, Switzerland), rabbit anti-glial-fibrillary-acidic-protein (GFAP, a mature and reactive glial cell marker, 1:1000–1:8000; Dako, Glostrup, Denmark), rabbit anti-BLBP (radial glial marker, 1:1000–1:8000; Chemicon, Temecula, CA, USA), mouse anti-nestin (progenitor and radial glial marker, 1:250; Abnova Corp.), rat anti-F480 (macrophage marker, 1:1000; Chemicon), goat anti-MCT2 (1:1000; Santa Cruz Biotechnology, Delaware, CA, USA), goat anti-GPR81 (G-protein-coupled lactate receptor, 1:500; Santa Cruz Biotechnology), goat anti-Iba1 (microglial and macrophage marker, 1:200; Abcam, Cambridge, UK), rabbit anti-CX3CR1 (microglial and macrophage marker, 1:500; Abcam), rabbit anti-Ki67 (cell cycle marker, 1:500; Abcam), goat anti-actin (cytoskeletal marker, 1:2000; Santa Cruz Biotechnology), mouse anti-Tuj-1 (neuronal marker, 1:10,000; Covance, Princeton, NJ, USA), rabbit anti-MAP2 (neuronal cell bodies and dendritic marker, 1:2000; Covance), rabbit anti-doublecortin (DCX, neuronal marker, 1:1000; Abcam), goat anti-FOXP2 (progenitor marker, 1:1000; Santa Cruz Biotechnology), rabbit anti-Pax6 (bipotential radial glial marker, 1:250; Abcam), rabbit anti-Tbr2 (neurogenic intermediate progenitor cell marker, 1:500; Abcam), rabbit anti-Sox2 (stem cell marker, 1:1000; Abcam), rat anti-CD31/PECAM (endothelial marker, 1:200; Abnova Corp.), rabbit anti-laminin (extracellular matrix and blood vessel marker, 1:500; Sigma–Aldrich), rabbit anti-NG2 (oligodendrocyte precursor cells, 1:1000; Chemicon), rabbit anti-olig2 (oligodendrocyte transcription factor 2, 1:200; Abcam), rabbit anti-PSD95 (postsynaptic marker, 1:1000; Abcam), or mouse anti-SNAP25 (presynaptic marker, 1:1000; Covance).

2.8. BrdU labeling

Starting at different time points after scaffold implantation, 5-bromo-2′-deoxyuridine (BrdU, Sigma–Aldrich) was injected intraperitoneally (5 mg/10 gr body weight) every 24 h for a 5-day period. BrdU incorporation was analyzed by immunohistochemistry (rat-anti-BrdU, 1:1000; Abcam) at different time points after injection. The injection protocol was as follows (in which P indicates postnatal day): P6: 3 h after the first injection ($n = 5$); P11: injections at P6–P10 ($n = 5$); at 1 year: injections at P6–P10 ($n = 3$); at 1 year: injections at 2 months ($n = 3$); at 1 year: injections one week before death ($n = 3$). The cell types that incorporated BrdU and their progeny were identified by double immunohistochemistry with BrdU antibodies and antibodies to Sox2, Tbr2, Pax6, DCX, NeuN, PV, GFAP, and olig2.

2.9. Vascular labeling

The lipophilic carbocyanine dye DiI (Sigma–Aldrich) was injected during cardiac perfusion of the animals, as previously described [25]. DiI-labeled vasculature was reconstructed on 300-μm-thick coronal sections ($n = 4$ aligned nanofibers; $n = 3$ random nanofibers). Vasculature staining with 1 mg/ml *Lycopersicon esculentum* (tomato) FITC-conjugated lectin (Sigma–Aldrich) was performed by caudal vein perfusion according the following protocol (http://werblab.ucsf.edu/sites/werblab.ucsf.edu/files/protocol%20pdfs/Lectin_perfusion.pdf).

2.10. Retrograde neural tracing studies

One year after scaffold implantation, cholera toxin subunit B conjugated to Alexa fluor 555 (AF-CBT) was stereotactically injected as described [26] into the intact contralateral somatosensory cortex of the mice. Control animals ($n = 2$) and radial scaffold implanted animals ($n = 4$) were killed after 4 days and their brains were analyzed.

2.11. Imaging and cell analysis

Cells were observed *in vivo* using an Axiovert 40 CFL light-inverted microscope (Carl Zeiss, USA). Digital images were acquired throughout the experiments using a digital camera controlled by software. Fluorescent preparations were viewed and micrographs were taken with either a Leica TCS-SL spectral confocal microscope (Leica Microsystems, Mannheim, Germany) or a Nikon Eclipse 800 light microscope (Nikon, Tokyo, Japan). Images were assembled in Adobe Photoshop (v. 7.0), with adjustments for contrast, brightness, and color balance to obtain optimum visual reproductions. Morphometric, quantitative, and live-image analyses were performed using ImageJ software (National Institutes of Health, USA).

Confocal images were reconstructed using the Imaris program (Bitplane, Zurich, Switzerland) for 3D and 4D real-time interactive data viewing, with normal or shadow projections of coronal tissue sections screened under a Leica TCS-SL spectral confocal microscope.

2.12. Magnetic resonance imaging (MRI)

MRI experiments were conducted on a 7.0 T BioSpec 70/30 horizontal animal scanner (Bruker BioSpin, Ettlingen, Germany) equipped with a 12-cm inner diameter actively shielded gradient system (400 mT/m). The receiver coil was a phased-array surface coil for mouse brain. The mice were placed in a supine position in a Plexiglas holder fitted with a nose cone for administering anesthetic gases (iso-fluorane in a mixture of 30% O_2 and 70% CO_2) and secured using a tooth bar, ear bars, and adhesive tape. Tripilot scans were used for accurate positioning of the animal's head in the isocenter of the magnet. High-resolution T2-weighted images were acquired using TurboRARE (rapid acquisition with rapid enhancement) sequences, with a repetition time = 2970 ms, echo time = 12 ms, RARE factor = 8, 10 averages, slice thickness = 0.3 mm, 25 slices for axial view and 40 slices for sagittal view, field of view = 25 × 25 mm, matrix size = 240 × 240 pixels, resulting in a spatial resolution of 0.104 × 0.104 mm for a slice thickness of 0.3 mm.

2.13. Statistical analyses

Statistical analyses were performed using Statgraphic-plus software. One-way ANOVA and Fisher's least significant difference (LSD) procedure were used to distinguish the means. Statistical significance was set at $P < 0.05$ (*) and $P < 0.001$ (**).

3. Results

3.1. Effect of PLA nanofibers on neuronal and glial cultures

The production of 238 ± 18-μm nanofiber sheets with the PLA nanofibers in two different conformations, random and aligned, was successfully achieved by the electrospinning method (Fig. 1A, B). We obtained continuous and homogeneous fiber thicknesses (657 ± 101 nm for random and 568 ± 81 nm for aligned nanofibers), with no bead content. Focused ion beam cross-sectional images of an aligned fibrous sheet (Fig. 1B inset) showed that the nanofibers were hollow (~500 nm inner diameter) because of the Kirkendall effect [27]. On AFM imaging, the single aligned nanofibers were smooth (RMS value of 14.2 ± 0.3 nm) (Fig. 1C) and relatively soft (DMT modulus of 3.0 ± 0.004 MPa) (Fig. 1D). Tensile strain differed between the two conformations. Thus, the Young's modulus of the random nanofibers was isotropic (41.4 ± 13.7 MPa) while the aligned nanofibers showed an anisotropic Young's modulus almost four-fold higher, as determined in a uniaxial assay parallel to the direction of the nanofibers (142.7 ± 14.1 MPa; Fig. 1H). The amorphous nature of the nanofibers was characterized by XRD (Fig. 1E) and DSC (Fig. 1F), neither of which showed evidence of crystallization or melting peaks, indicating a nearly null crystallinity. Both PLA fiber conformations were hydrophobic (contact angle of 137° ± 14° for aligned and 128° ± 17° for random conformations) and negatively charged (ζ-potential at pH 7.4 = −41 ± 43 mV) and the degradation rates were similar (νLac-random = 458 nM·h-1 and νLac-aligned = 467 nM·h-1) (Fig. 1G). However, it should be taken into account that the enzymatic reaction indicative of degradation only allows the detection of L-lactate monomers. Soluble PLA oligomers and D-lactate monomers are undetectable by this technique.

For cell culture, uncoated random and aligned fiber sheets were used as the substrates. Neurons and glial cells were identified by their immunoreactivity to β-III tubulin (Tuj-1) and BLbP, respectively [28]. On random scaffolds, neurons and glial cells grew on the surface and adopted multipolar shapes (Fig. 2A), while in aligned scaffolds they were bipolar, oriented in the fiber direction, and invaded the entire thickness (Fig. 2B–D). Neuronal migration in PLA nanofibers was analyzed by video time-lapse microscopy, which showed the adherence of embryonic neurons to single nanofibers and their migration alongside them (Supplementary video 1), mimicking neuronal behavior on radial glia during brain development [14].
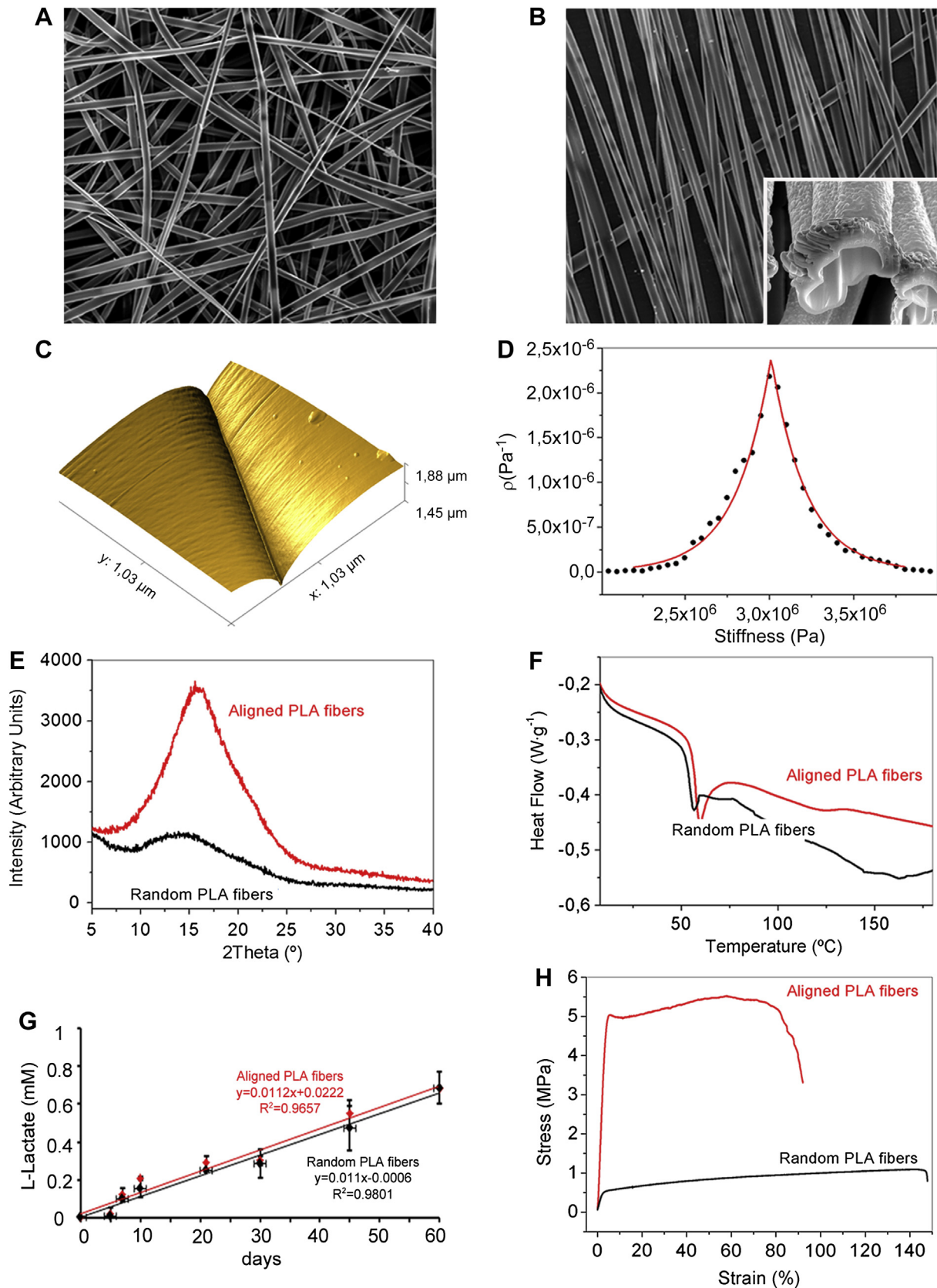
Fig. 1. Material characterization. (A, B) Field emission scanning electron microscopy images of **(A)** random and **(B)** aligned nanofibers viewed from above, with a cross-section of aligned nanofibers produced by focused ion beam shown in the inset in **B**. **(C)** Atomic force microscopy (AFM) topographic plot of the interface of two parallel nanofibers (RMS value of 14.2 ± 0.3 nm). Stiffness value distribution based on **(D)** the DMT modulus measured by AFM, showing a peak at 3.01 ± 0.004 MPa, and **(E)** X-ray diffraction. **(F)** Differential scanning calorimetry spectra of random (black) and aligned (red) nanofiber conformations, showing the amorphous nature of the fibers. **(G)** Plot of lactate release vs. time of random (black, vLac-random = 458 nM h^{-1}) and aligned (red, vLac-aligned = 467 nM h^{-1}) nanofiber sheets. **(H)** Mechanical assays after tensile loading of the two nanofiber conformations. Scale bars: 5 μm **(A, B)**; 500 nm **(B inset)**. (For interpretation of the references to color in this figure legend, the reader is referred to the web version of this article.)
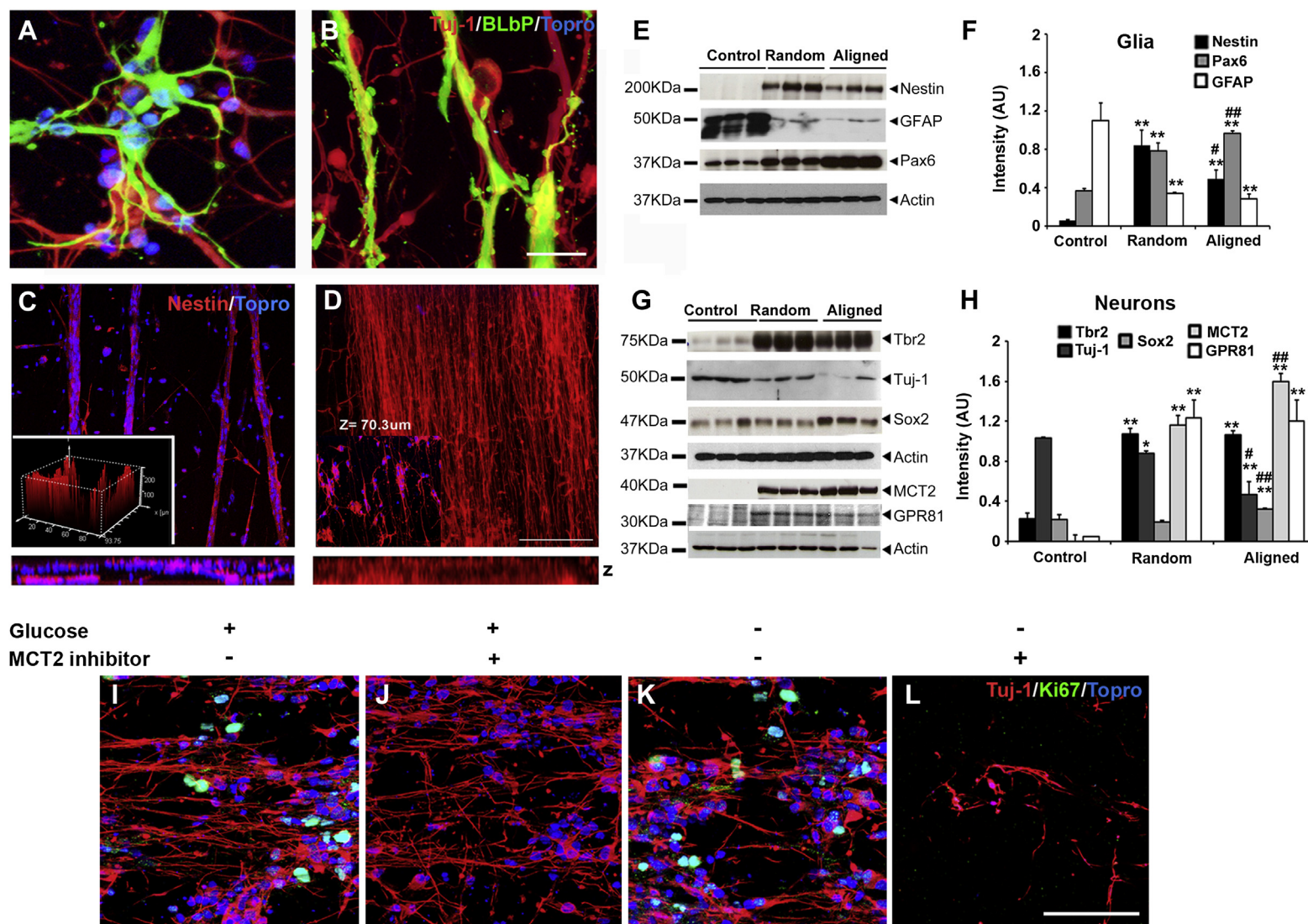
Fig. 2. Lactate released by PLA nanofibers induces radial glia and neurogenic progenitors. (A, B) Morphology of BLbP+ glia (green) and Tuj-1+ neurons (red) on random **(A)** and aligned **(B)** nanofibers after 10 div. Confocal images of **(C)** glial cells stained with nestin (red) and **(D)** neurons stained with Tuj-1 (red) on aligned PLA nanofibers after 5 div. Glial cells colonized an area of 200 μm in the z plane of the scaffold **(C, inset)** while neuronal somas localized in the middle of the scaffold **(D, inset)**. Western blots show the expression of nestin, Pax6, and GFAP markers in glial cell cultures **(E)** and of Tbr2, Tuj-1,Sox2, MCT2 and GPR81 in neuronal cultures **(G)** after 5 div. **(F, H)** Western blot densitometry (intensity values normalized to actin). **(I–L)** Confocal images of neuronal cultures grown on aligned nanofibers in NB medium **(I, J)** or in glucose-free NB-A medium **(K, L)** after 5 div in the presence or absence of AR-C155858, an inhibitor of monocarboxylate transporters (MCT) 1/2. Neurons are stained with Tuj-1 antibody (red) and proliferative cells with Ki67 (green). Nuclei are stained with TOPRO-3 (blue).*$P < 0.05$, **$P < 0.001$, LSD test (compared with control); #$P < 0.05$, ##$P < 0.001$, LSD test (random vs. aligned nanofibers), $n = 5$. Scale bars: 20 μm **(A, B)**; 100 μm **(C, D)**; 50 μm **(I–L)**. (For interpretation of the references to color in this figure legend, the reader is referred to the web version of this article.)
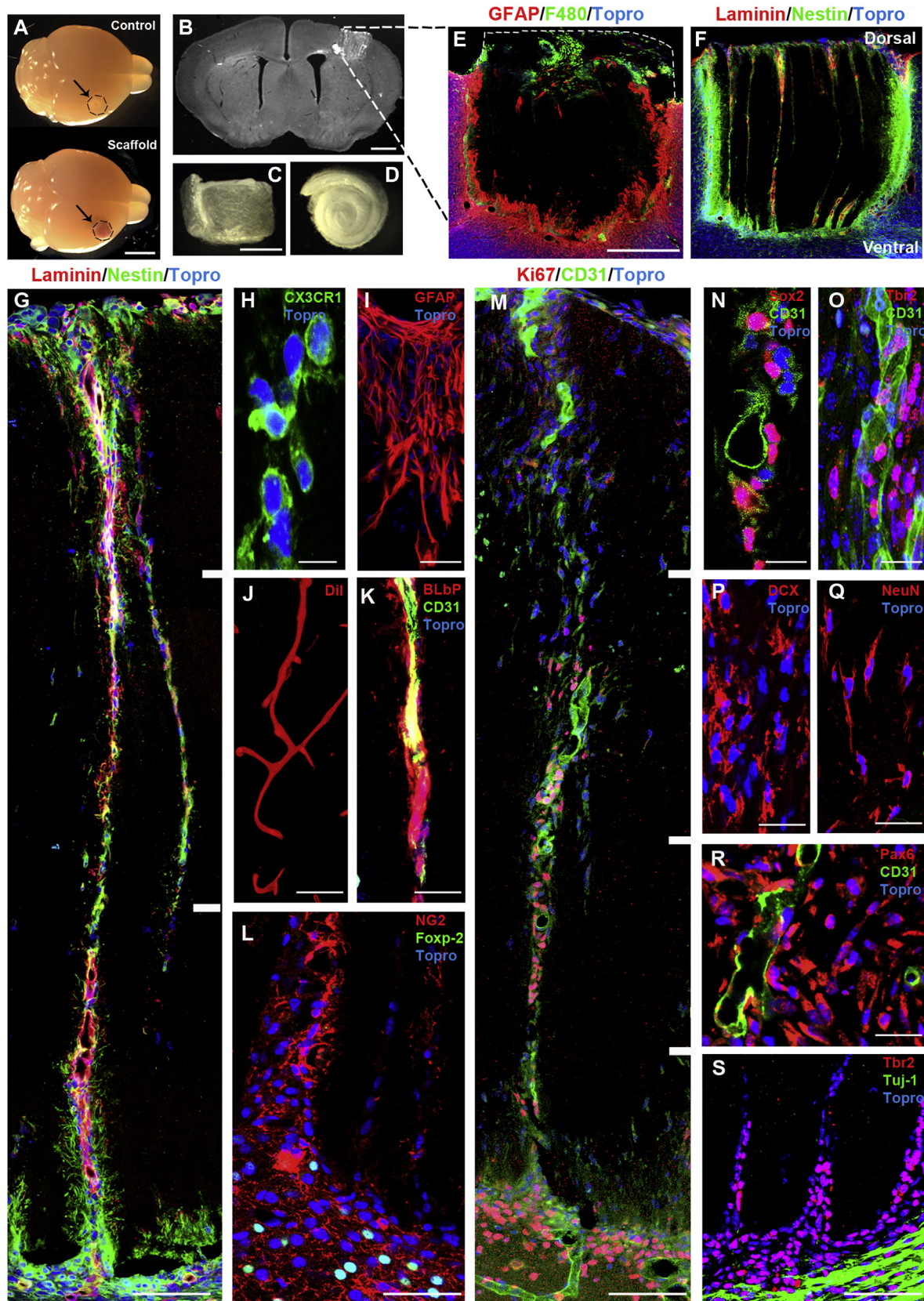
Fig. 3. Neurovascular bridges inside radial scaffolds. (A) Macroscopic view of postnatal day 11 (P11) mouse brains with control injury (Control) or with an implanted PLA scaffold (Scaffold) in the right cortex. **(B)** Bright-field coronal section showing the implanted radial scaffold. **(C, D)** Lateral and top views of the scaffold before implantation. Confocal images showing **(E)** GFAP+ astroglia (red) and F480+ macrophages (green) surrounding the scaffold and **(F)** nestin+ radial glia (green) and laminin basal lamina (red) forming radial neurovascular bridges inside the scaffold. **(G)** High magnification of **(F)**, showing a neurovascular bridge reconnecting basal and meningeal zones. **(H, I)** Higher magnifications show resolving macrophages stained with CX3CR1 (green) **(H)** and GFAP+ astroglia (red) **(I)** in the upper third of the implant. **(J)** Functional blood vessels stained by DiI perfusion. **(K)**

Supplementary video related to this article can be found at http://dx.doi.org/10.1016/j.biomaterials.2014.02.051.

The expression of cell-type molecular determinants of neurogenic niches [29–31] was then analyzed by immunocytochemistry and western blot. After 5 div on PLA fiber scaffolds, glial cultures dramatically increased their expression of the radial glia markers nestin and Pax6 and decreased their expression of the astroglial marker GFAP (Fig. 2E, F). Similarly, compared to control cultures, neuronal cultures on PLA fiber scaffolds dramatically increased their expression of Ki67+ cycling progenitors, the neuronal progenitor marker Tbr2, and the NSC marker Sox2, whereas expression of the post-mitotic neuron marker Tuj-1 was lower (Fig. 2G, H, Supplementary Fig. 1). Moreover, in contrast to random scaffolds, aligned scaffolds better reproduced neurogenic niche properties, as the expression of both Sox2 and Pax6 increased significantly (Fig. 2F, H).

In neuronal cultures, lactate released from PLA scaffold degradation induced a large increase in MCT2 and GPR81 (Fig. 2G, H). Next, neuronal cultures were grown on aligned nanofibers with or without glucose in the medium and treated with AR-C155858, an inhibitor of MCT1/2 [32] that blocks lactate entrance into cells. Pharmacological blockade of lactate transport induced KI67+ progenitor depletion even in the presence of glucose, and neuronal death in the absence of glucose (Fig. 2I–L). Thus, lactate released by PLA nanofibers apparently acts as an alternative fuel for neurons and is required for NSC/progenitor maintenance.

3.2. Implantation of PLA fiber scaffolds in vivo

During the first postnatal week, cortical gliogenesis is still very active whereas neurogenesis is mostly completed prenatally [33], with the exception of life-span neurogenesis in adult neurovascular niches [34]. To analyze the regenerative potential of PLA fiber scaffolds in vivo, we used a model of traumatic brain injury in 4-day-old (P4) mice. One-mm^3 random (random scaffolds, $n = 29$) and aligned PLA fiber scaffolds (aligned scaffolds, $n = 87$) following the radial orientation of radial glia (radial scaffolds, $n = 77$) or placed orthogonal to the orientation of radial glia (orthogonal scaffolds, $n = 10$) were fitted into the brain cavity just after tissue removal (Fig. 3A–D). The brains were then analyzed at 2 and 7 days and at 2, 6, and 12–15 months post-surgery. The non-implanted brain cavities (control, $n = 20$) remained empty, with no sign of brain tissue regeneration even 15 months after surgery (Supplementary Fig. 2). By contrast, despite evident signs of fiber degradation, the PLA fiber scaffolds were clearly visible 15 months after implantation (Supplementary Fig. 2). Since the amount of new tissue generated inside the radial scaffolds increased over time, most of the data reported below correspond to post-implantation days and to the experiment's end-point at 12–15 months. Abnormal neurological behavior was not observed in any experimental group or in mice of any age.

3.3. Brain tissue regeneration inside PLA fiber scaffolds in vivo

Brain tissue regeneration was assessed by immunofluorescence microscopy. One week after surgery, immune system activation was shown by the presence of F480+ mature macrophages at the border of the lesion site and at the tissue−implant interface (Fig. 3E). CX3CR1+ resolving macrophages [35] were also seen at the border and entering radial scaffolds from the meninges (Fig. 3H). Immune activation was residual after 1 year, with scarce F480+ macrophages at the tissue−implant interface (Supplementary Fig. 2B) and a few Iba1+ ramified resting microglia inside the radial scaffolds (Fig. 4M). One week after surgery, GFAP+ activated astrocytes were detected at the border of the lesion site and at the tissue−implant interface (Fig. 3E, I). At this time, nestin+ radial glia dramatically increased around and inside the aligned scaffolds, as did laminin, an adhesive extracellular matrix glycoprotein mainly secreted by glial and endothelial cells (Fig. 3F; Supplementary Fig. 2A). Newly generated tissue formed neurovascular bridges that crossed the scaffolds, following radial (Fig. 3F) or orthogonal (Supplementary Fig. 2A) trajectories to the brain surface, depending on the disposition of the aligned nanofibers. At this early time point, embryonic neurons expressing the transcription factors Foxp-2 [36] and Bhlhb5 (not shown) and Tuj1+ axons from the surrounding tissue were excluded from entering the scaffold (Fig. 3L, S). After 1 year, the initially narrow neurovascular bridges had formed large areas of regenerated tissue, containing blood vessels, neurons, and glial cells, inside the radial scaffolds (Fig. 4). Nestin+ and GFAP+ glial cells were abundant and widely distributed inside the scaffolds, maintaining the elongated shape and radial organization of embryonic radial glia and a laminin-rich extracellular matrix (Fig. 4C, D, J; Supplementary Fig. 2B). By contrast, in random scaffolds, despite similar fiber composition and size, these cells were only present at the tissue−implant interface (Supplementary Fig. 2B). Therefore, in subsequent experiments we used radial scaffolds for brain regeneration studies and random scaffolds as controls.

At the cell level, neurovascular bridges were organized around a central blood vessel formed by CD31+ endothelial cells [34] surrounded by a laminin-rich basal lamina (Fig. 3G, M). Glial populations around central vessels included nestin+ and BLbP+ radial glia (Fig. 3G, K; Supplementary video 2) and a heterogeneous population of NG2+ cells (Fig. 3L), including oligodendrocyte progenitors [9], while olig2+ oligodendrocytes were absent. The same populations persisted after 1 year, at which time olig2+ oligodendrocytes were also observed inside the scaffold (Fig. 4J, K, N). Transcardiac perfusion with the lipophilic tracer DiI revealed an effective connection between this radial vascular network inside the scaffold and the host vasculature as well as the perfusion of the newly formed vessels (Fig. 3J). At 1 year, DiI perfusion delineated large radial vessels that entered the radial scaffold before profusely branching (Fig. 4G, P; Supplementary video 3). This vascular organization closely reproduced the normal organization of blood vessels in the contralateral brain tissue (Supplementary video 4) whereas inside random scaffolds a similar vasculature was completely absent (Supplementary video 5).

Supplementary video related to this article can be found at http://dx.doi.org/10.1016/j.biomaterials.2014.02.051.

The regeneration of neurogenic niches inside radial scaffolds was also analyzed. After one week, Ki67+ cycling cells were found in close association with blood vessels in the tissue surrounding the scaffold and in the neurovascular bridges (Fig. 3M). The analysis of progenitor determinants revealed a highly heterogeneous population of neuronal and glial progenitors. The distribution of Sox2+ NSC, Pax6+ bipotential radial glia, and Tbr2+ neuronal restricted progenitors was similar to that of Ki67+ cells (Fig. 3M−O, R, S; Supplementary Fig. 3) and was maintained after 1 year. A functional

Proximity of BLbP+ radial glia (red) and CD31+ endothelial cells (green). **(L)** NG2+ cells (red) entering the scaffold and FOXP-2+ neurons (green) remaining in the lower layers. **(M)** CD31+ endothelial cells (green) in a neurovascular bridge surrounded by Ki67+ cycling progenitors, by Sox2+ stem cells (red) **(N)**, and by Tbr2+ neurogenic progenitors (red) **(O)**. **(P)** DCX+ and **(Q)** NeuN+ immature neurons. **(R)** CD31+ endothelial cells (green) surrounded by Pax6+ bipotential progenitors (red). **(S)** Tbr2+ progenitors (red) entering the scaffold and Tuj-1+ axons (green) at the material−tissue interface. Nuclei were stained with TOPRO-3 (blue). Scale bars: 2 mm **(A)**; 1 mm **(B)**; 500 μm **(C, D)**; 400 μm **(E, F)**; 50 μm **(G, M, S)**; 20 μm **(I, K)**; 10 μm **(H, J, L, N−R)**. (For interpretation of the references to color in this figure legend, the reader is referred to the web version of this article.)
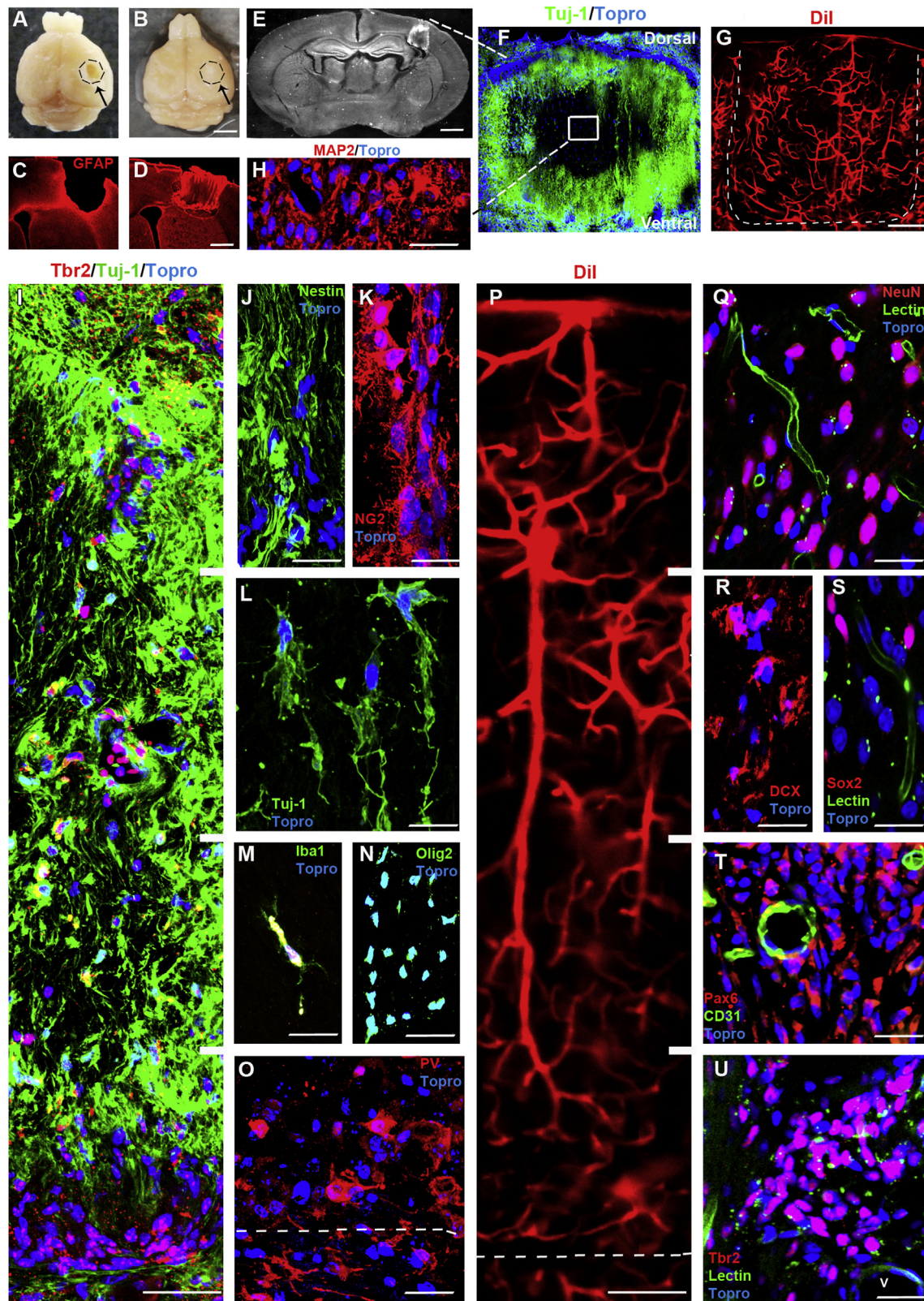
Fig. 4. **Extent of brain tissue regeneration and vascularization after 1 year.** Macroscopic view of brains with (**A**) control lesions and (**B**) radial scaffolds 1 year after implantation. Coronal sections showing GFAP+ astroglia around (**C**) a control lesion and (**D**) in the radial scaffold. (**E**) Bright-field coronal section showing the material remaining. (**F**) Magnification showing extensive colonization by Tuj-1+ neurons and (**G**) blood vessels labeled by DiI perfusion. (**H**) Mature neurons stained with MAP-2 in the middle of the scaffold. (**I**) Magnification of (**F**), showing Tuj-1+ neurons (green) and Tbr2 neural progenitors (red) following the radial organization of the nanofibers. Nestin+ radial glia (**J**), NG2+ cells (**K**), and Tuj-1+ neurons (**L**) in the middle of the scaffold. (**M**) Iba-1+ ramified microglia. (**N**) Olig2+ oligodendrocytes. (**O**) PV+ GABAergic neurons on both sides of the tissue−scaffold interface. (**P**) Reconstruction at 300 μm of blood vessels perfused with DiI inside an aligned scaffold. (**Q**) The vicinity of NeuN+ neurons (red) and the microvasculature labeled by lectin perfusion (green). (**R**) DCX+ immature neurons. (**S−U**) Lectin/CD31+ blood vessels (green) surrounded by Sox2+ stem cells (red) (**S**), Pax6+ bipotential progenitors (red) (**T**), and Tbr2+ neural progenitors (red) (**U**). Nuclei were stained with TOPRO-3 (blue). Scale bars: 1 mm (**A, B**); 500 μm (**C, D**); 1 mm (**E**); 200 μm (**F, G**); 25 μm (**H, J, P, O**); 20 μm (**J, K, L, Q−U**); 10 μm (**M, N**). (For interpretation of the references to color in this figure legend, the reader is referred to the web version of this article.)

microvasculature associated with the neurogenic niche was revealed by CD31 expression or tomato lectin perfusion through the caudal vein. NSCs and progenitors expressing Sox2, Pax6, or Tbr2 (Fig. 4I, S–U) were present inside radial scaffolds in close association with tomato-lectin-labeled microvasculature.

Finally, immature bipolar neurons expressing DCX, a microtubule-associated protein required for neuronal migration, and the neuronal transcription factor NeuN [37] were also detected in the neurovascular bridges after 1 week (Fig. 2P, Q; Supplementary Fig. 3). DCX+ immature neurons were still present after 1 year (Fig. 4R), at which time neurons expressing Tuj-

1 (Fig. 4F, I, L), MAP-2 (Fig. 4H), and nuclear NeuN (Fig. 4Q) were abundant and formed a rich neuronal meshwork (Fig. 4F, H). Some GABAergic neurons that stained with PV and had a well-developed morphology were also found inside the scaffold (Fig. 4O).

Taken together, these results indicate that neither a foreign body reaction nor encapsulation were elicited by the implanted scaffold. Radial scaffolds were invaded by vascular sprouts, radial glia, and neural progenitors during the first week, suggesting that the neurogenic neurovascular niches were reconstituted early on inside the scaffolds and were still active after 1 year.
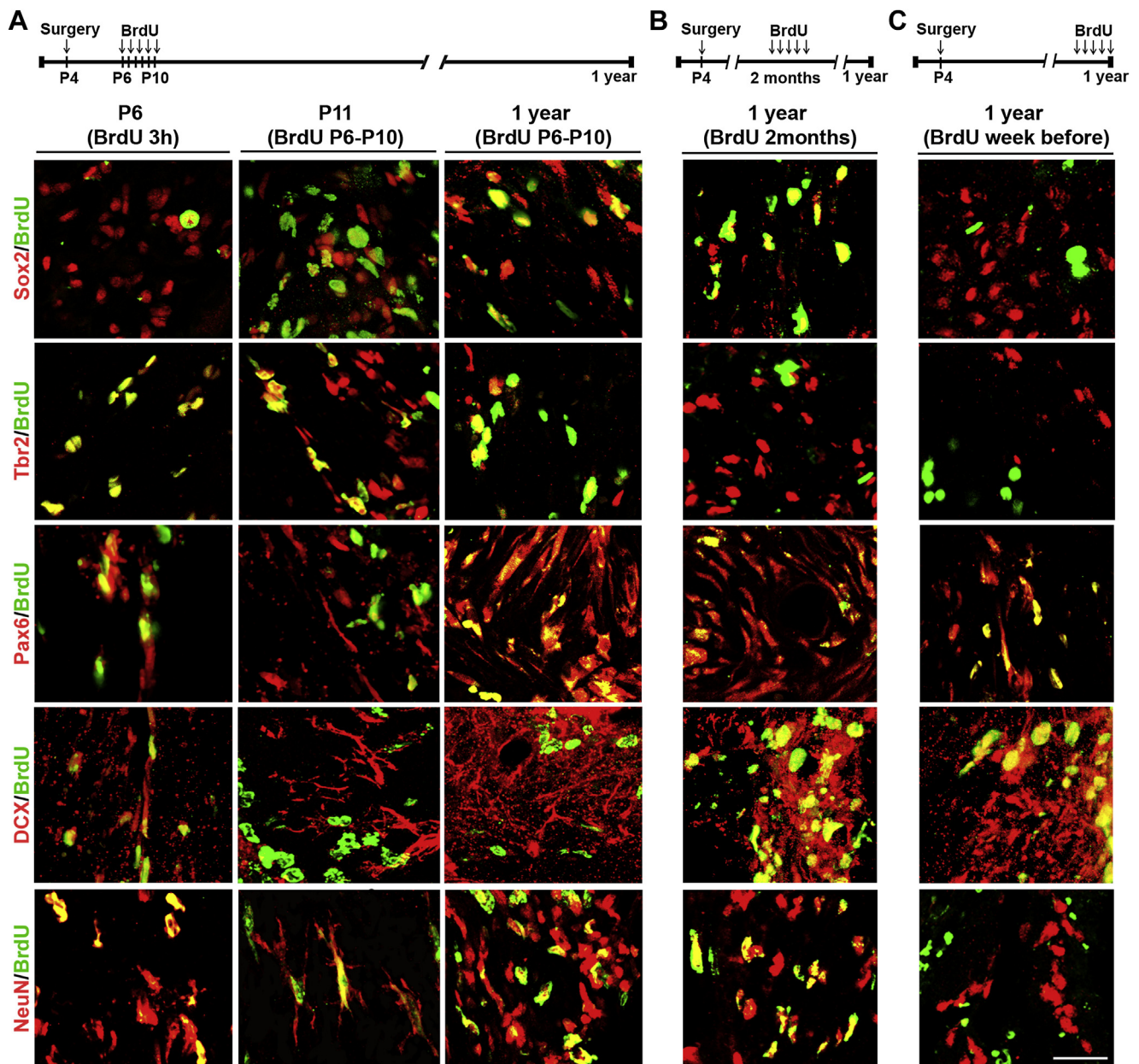

Fig. 5. BrdU incorporation into NSC/progenitors and neurons inside radial scaffolds. BrdU immunostaining (green) and colocalization inside the implant with molecular markers (red) of stem cells (Sox2), neuron-restricted progenitors (Tbr2), bipotential progenitors (Pax6), and neurons (DCX, NeuN). **(A)** BrdU was injected intraperitoneally for 5 consecutive days, from P6 (2 days after scaffold implantation) to P10, and then analyzed 3 h after the first BrdU injection, 7 days after implantation (P11), and 1 year after implantation. **(B)** BrdU was injected intraperitoneally for 5 consecutive days 2 months after implantation and analyzed at 1 year. **(C)** BrdU was injected intraperitoneally for 5 consecutive days 1 year after implantation and analyzed the day after the last injection. Scale bar: 20 μm. (For interpretation of the references to color in this figure legend, the reader is referred to the web version of this article.)
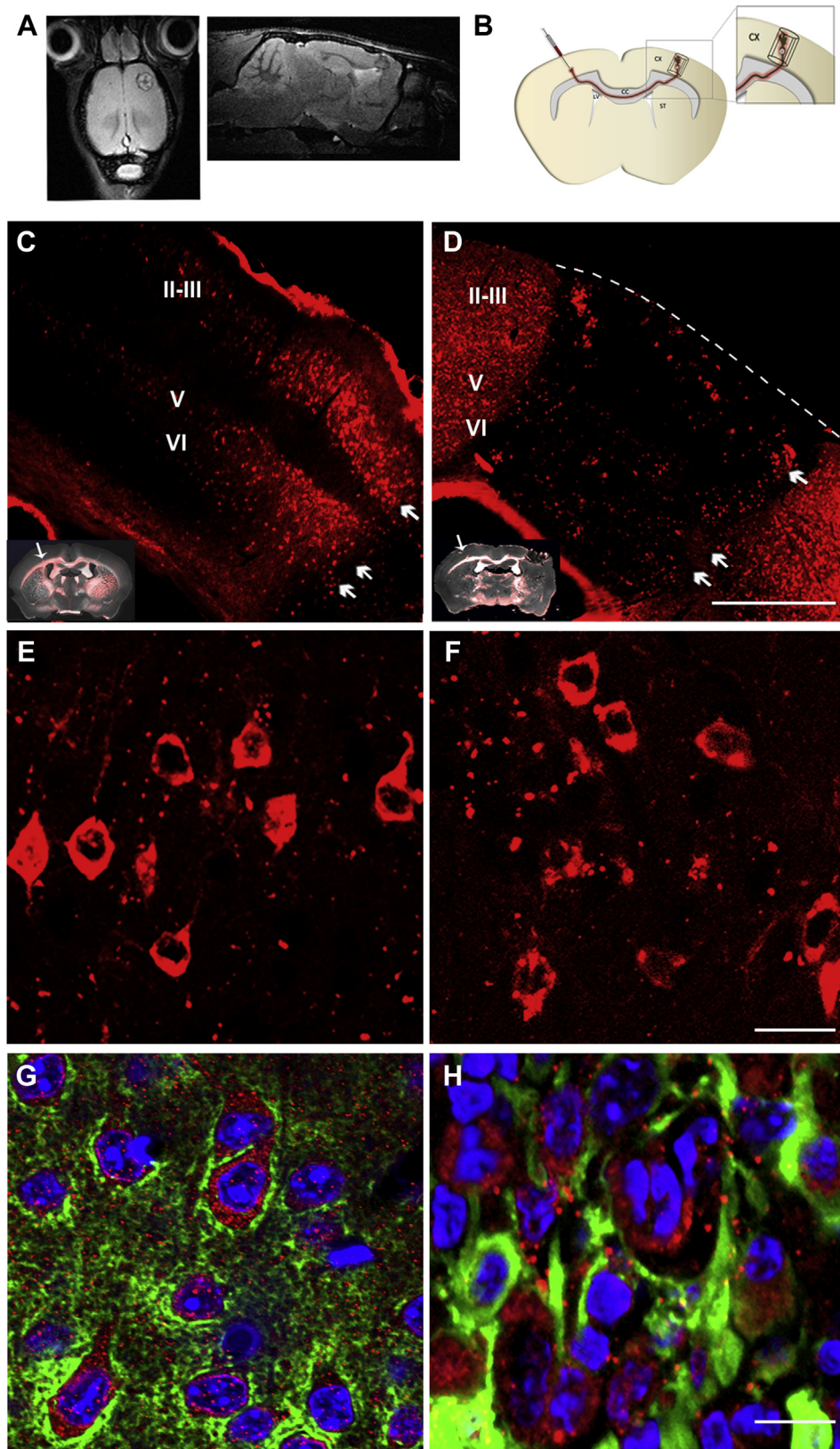
Fig. 6. Functional integration of newly generated neurons in radial scaffolds. (A) Horizontal and parasagittal MRI showing the integration of a radial scaffold 1 year after implantation. (B) Diagram of the retrograde tracing of commissural neurons following the injection of AF-CBT in the contralateral cortex of the radial scaffold implant. (C) Distribution of AF-CTB labeled commissural neurons (arrows) in the contralateral hemisphere of an uninjured control brain and inside a radial implant (D). Insets in (C) and (D) are superimposed images of differential interference contrast and fluorescence (red), showing the exact area of AF-CTB injection (arrow). (E, F) Magnification showing retrograde-labeled pyramidal neurons in the contralateral hemisphere to the injection in a control (E) and in an implanted (F) brain. (G, H) Presynaptic SNAP25 (green) and postsynaptic PSD95 (red) labeling in control cortex (G) and inside a radial scaffold 1 year after implantation (H). Cortical layers II–III, V, VI. Scale bars: 250 μm (C, D); 20 μm (E, F); 10 μm (G, H). (For interpretation of the references to color in this figure legend, the reader is referred to the web version of this article.)

3.4. Neurogenesis and neuronal differentiation inside radial scaffolds

To confirm the activity of neurogenic niches, we examined the fates of dividing cells using markers for DNA replication (BrdU, a thymidine analog) and progressive neuronal differentiation. At the time of implantation (P4), BrdU was incorporated in cells mostly located in the ventricular zone/subventricular zone (VZ/SVZ) and in a few cells scattered through the cortex. Only a few cells were double-labeled with BrdU and Sox2, Tbr2, Pax6, or DCX, while extensive BrdU and NeuN colocalization was seen in SVZ neuroblasts (Supplementary Fig. 4). When injected during the first week after surgery (1 injection/day for 5 days, P6–P11), BrdU was incorporated dramatically around and inside the radial scaffold (Fig. 5A), but not on the contralateral side (Supplementary Fig. 5). Three hours after the first injection (P6), BrdU was found in progenitors expressing Tbr2 and Pax6 and in neuroblasts expressing DCX and NeuN. Only a few Sox2+ NSCs incorporated BrdU, but their number increased at P11, after 5 consecutive injections, suggesting the slow cycling of these progenitors. In the regenerated tissue, BrdU persisted in Sox2, Tbr2, and Pax6 progenitors for more than 1 year, indicating that they underwent very few rounds of cell division. After 1 year, abundant DCX+ or NeuN+ neurons (Fig. 5A) and some PV+ GABAergic neurons, GFAP+ astrocytes, and olig2+ oligodendrocytes (Supplementary Fig. 6) co-localized with the BrdU inside the scaffold. These data were consistent with both extensive neurogenesis and gliogenesis soon after radial scaffold implantation and the long-term survival of the newly generated neurons and glial cells. When BrdU was injected 2 months after radial scaffold implantation, it was incorporated into Sox2+ and Pax6+ progenitors and into DCX+ and NeuN+ neurons (Fig. 5B), whereas when injected at 1 year it was seen only in Pax6+ progenitors and DCX+ and NeuN+ neurons (Fig. 5C). These data suggest that substantial neurogenesis continues in the implant, although the progenitor types and generated neurons probably vary.

Implant integration into the surrounding tissue was assessed by MRI in a group of mice (n = 8). Six to 12 months after implantation, the meninges and skull had regenerated and the scaffold limits were clearly visible in the right motor/somatosensory cortex. Signal intensity inside the implant was similar to that in the surrounding tissue (Fig. 6A). Unfortunately, the system's limits of resolution in mice did not permit functional MRI. Instead, integration of the newly generated neurons inside the radial scaffold into brain circuitry was analyzed by retrograde tracing of commissural neurons 1 year after implantation. AF-CTB was injected into the contralateral hemispheres of mice with implanted radial scaffolds (Fig. 6B) and of uninjured control animals. Four days after AF-CTB injection, retrograde transport of the tracer through the corpus callosum was evident, as was the staining of two bands of pyramidal neurons in layers VI–V and II–III in control animals (Fig. 6C, E). Many retrogradely labeled pyramidal neurons were also found inside radial scaffolds, with a distribution that suggested a certain degree of anatomical and functional laminar organization within the regenerated tissue (Fig. 6D, F), as inside the scaffold they roughly reproduced the normal bilaminar distribution of callosal neurons [38]. The presence of a functional synaptic machinery in the regenerated tissue was confirmed by the immunohistochemical detection of postsynaptic density protein 95 (PSD95) and synaptosomal-associated protein 25 (SNAP25). Both proteins were expressed in neurons inside the regenerated tissue and their distribution resembled that in the adult cortex (Fig. 6G, H).

4. Discussion

Our results demonstrate that lactate-releasing PLA70/30 radially aligned fiber scaffolds reproduce some of the organizational and functional aspects of the embryonic NSC niche, including induction of the robust and sustained generation of several types of neurons and glial cells, and accompanied by complete vascularization of the implant. The new neurons survived for more than 1 year and differentiated inside the scaffold, receiving synapses and sending axons that became integrated into functional brain circuits.

Several different mechanisms might cooperate in driving the reactivation of embryonic neurogenic and angiogenic programs by lactate-releasing PLA nanofiber scaffolds. First, the present and previous data demonstrated that PLA70/30 and L-lactate are required to maintain the metabolism and self-renewal of neurogenic progenitors [22,23] and both induce angiogenesis [21]. Second, PLA nanofibers are hydrophobic, with the same size, shape, and negative superficial charge as radial glia shafts [19,39]. Accordingly, the surface properties of PLA nanofibers may well be similar to those of negatively charged lipids on the surface of astrocytes and radial glia, controlling the extracellular polymerization of laminin [39], an intrinsic component of the extracellular matrix of neurogenic NSC niches [40]. Laminin was strongly up-regulated in cells around and inside the scaffold. The appropriate orientation of vascular sprouts and radial glia in the regenerating tissue was only achieved when the topology of the PLA nanofibers reproduced that of embryonic radial glia organization. Random PLA nanofibers did not allow vascular invasion inside the scaffold, demonstrating the relevance of scaffold topology in CNS regeneration. The robust functional vascularization induced by aligned PLDLA nanofibers contrasts with the poor vascularization reported when aligned PLA (pure L isomer) microfibers were implanted into the transected spinal cord [41]. The principal difference between the two fiber types is that mismatching of the chains in PLDLA results in less order, less crystallinity, and a higher degree of amorphicity, and therefore, a higher polymer degradation rate. It is known that lactate is a common cue that supports neuronal and NSC/progenitor metabolism [22,23] and induces angiogenesis in the presence of glucose and fluctuating oxygen levels [21]. Taken together, these data indicate that topology is necessary but not sufficient for vascularization and that lactate release is also a requirement. Recent studies similarly demonstrated that lactate-releasing radial glia are essential in guiding and stabilizing the nascent brain vascular network [42].

Laminin deposition around PLA fibers might also help in directing the formation of endothelial sprouts and the stabilization of new blood vessels inside the scaffold [43]. Moreover, interactions between laminin and its receptors in vascular cells, NSCs/precursors, and migrating neuroblasts are thought to regulate NSC/precursor activation and cell migration [44–46]. PLA scaffolds might also limit inflammation, by recruiting the CX3CR1+-resolving macrophages required for its resolution [35].

Another important question is the original lineage of the dedifferentiated neuronal progenitors. BrdU analyses indicated that the newly generated cells comprise a heterogeneous population of radial glia, NSCs, intermediate progenitors, neurons, and glial cells. The observed temporal changes in progenitor pool activation and in the neuronal and glial types that incorporated BrdU suggested that the contributions of the different progenitor types to neurogenesis differed throughout the life span of the implant. Neurogenic radial glia progenitors are a constant in embryonic and adult neurogenic niches [10,11]. In the newly lesioned brain, activated SVZ progenitors generate protective astrogenesis [47] and, to a much lesser extent, give rise to neurons that migrate and integrate into the subjacent cortex [18,37,48]. In our implants in neonatal mice, substantial vascular and progenitor invasion occurred from the meningeal and lateral sides; however, tissue regeneration was considerably reduced when the entire VZ/SVZ was surgically destroyed (data not shown), suggesting that these zones are an

important but not exclusive progenitor source. In addition, direct dedifferentiation of mature glia into neurogenic progenitors has been described after Sox2 transfection [49] and in response to extracellular cues [9,24]. Although the exact progenitor source of the newly generated neurons and glial cells remains unclear, our data suggest that progenitors with multiple origins and different time-dependent activation contributed to brain tissue regeneration in the radial PLA nanofiber scaffolds. The newly generated neurons were also functional, integrating into brain circuitry and establishing synaptic contacts, as demonstrated by retrograde AF-CTB labeling and the expression of pre- and postsynaptic proteins. Unfortunately, a direct demonstration of the functionality of the regenerated tissue was not possible due to technical limitations of functional MRI in mice and to mechanical interference of the implanted scaffold with the glass micropipettes required for electrophysiological recordings.

Finally, one of the undesirable associated risks of therapies based on cell reprogramming or dedifferentiation is the induction of neuroglial tumors. This possibility was carefully checked in the implanted animals and neither brain tumors nor the expression of CD133, a molecular marker of glioma-initiating cells [50], was found (data not shown).

5. Conclusions

This study demonstrated that biomimetic scaffolds consisting of radially aligned electrospun PLA70/30 fibers release L-lactate and reproduce the 3D organization and supportive function of embryonic radial glia, thus mimicking some of the physical and biochemical characteristics of the embryonic NSC niche. Radial scaffolds implanted into brain cavities induced robust and functional vascularization in the fiber orientation from 1 week to 15 months, neurogenesis for more than 1 year, and the survival and integration of the newly generated neurons into normal brain circuits. Although there is a long way to go before their clinical translation, our results open up unexpected and exciting perspectives in the design of cell-free implantable devices. By means of tuned biomaterials it may be possible to regulate biophysical and metabolic parameters to reproduce embryonic neurovascular niches inducing gliogenesis, neurogenesis, and vascularization, leading to the restoration of functional CNS tissue lost after a lesion without the need for exogenous cells, growth factors, or genetic manipulation.

Appendix A. Supplementary data

Supplementary data related to this article can be found at http://dx.doi.org/10.1016/j.biomaterials.2014.02.051.

References

[1] Bigler ED. Neuroinflammation and the dynamic lesion in traumatic brain injury. Brain 2013;136:9–11.

[2] Frontczak-Baniewicz M, Chrapusta SJ, Sulejczak D. Long-term consequences of surgical brain injury – characteristics of the neurovascular unit and formation and demise of the glial scar in a rat model. Folia Neuropathol 2011;49(3):204–18.

[3] Forraz N, Wright KE, Jurga M, McGuckin CP. Experimental therapies for repair of the central nervous system: stem cells and tissue engineering. J Tissue Eng Regen Med 2013;7:523–36.

[4] Orive G, Anitua E, Pedraz JL, Emerich DF. Biomaterials for promoting brain protection, repair and regeneration. Nat Rev Neurosci 2009;10:682–92.

[5] Bible E, Chau DY, Alexander MR, Price J, Shakesheff KM, Modo M. The support of neural stem cells transplanted into stroke-induced brain cavities by PLGA particles. Biomaterials 2009;30:2985–94.

[6] Park KI, Teng YD, Snyder EY. The injured brain interacts reciprocally with neural stem cells supported by scaffolds to reconstitute lost tissue. Nat Biotechnol 2002;20:1111–7.

[7] Volpato FZ, Fuhrmann T, Migliaresi C, Hutmacher DW, Dalton PD. Using extracellular matrix for regenerative medicine in the spinal cord. Biomaterials 2013;34:4945–55.

[8] Saha B, Jaber M, Gaillard A. Potentials of endogenous neural stem cells in cortical repair. Front Cell Neurosci 2012;6:14.

[9] Robel S, Berninger B, Gotz M. The stem cell potential of glia: lessons from reactive gliosis. Nat Rev Neurosci 2011;12:88–104.

[10] Weissman T, Noctor SC, Clinton BK, Honig LS, Kriegstein AR. Neurogenic radial glial cells in reptile, rodent and human: from mitosis to migration. Cereb Cortex 2003;13:550–9.

[11] Tanaka EM, Ferretti P. Considering the evolution of regeneration in the central nervous system. Nat Rev Neurosci 2009;10:713–23.

[12] Anthony TE, Klein C, Fishell G, Heintz N. Radial glia serve as neuronal progenitors in all regions of the central nervous system. Neuron 2004;41:881–90.

[13] Kriegstein A, Alvarez-Buylla A. The glial nature of embryonic and adult neural stem cells. Annu Rev Neurosci 2009;32:149–84.

[14] Rakic P. Developmental and evolutionary adaptations of cortical radial glia. Cereb Cortex 2003;13:541–9.

[15] Stubbs D, DeProto J, Nie K, Englund C, Mahmud I, Hevner R, et al. Neurovascular congruence during cerebral cortical development. Cereb Cortex 2009;19:32–41.

[16] Tam SJ, Watts RJ. Connecting vascular and nervous system development: angiogenesis and the blood-brain barrier. Annu Rev Neurosci 2010;33:379–408.

[17] Buffo A, Rolando C, Ceruti S. Astrocytes in the damaged brain: molecular and cellular insights into their reactive response and healing potential. Biochem Pharmacol 2010;79:77–89.

[18] Covey MV, Jiang Y, Alli VV, Yang Z, Levison SW. Defining the critical period for neocortical neurogenesis after pediatric brain injury. Dev Neurosci 2010;32:488–98.

[19] Anton ES, Marchionni MA, Lee KF, Rakic P. Role of GGF/neuregulin signaling in interactions between migrating neurons and radial glia in the developing cerebral cortex. Development 1997;124:3501–10.

[20] Baud O, Fayol L, Gressens P, Pellerin L, Magistretti P, Evrard P, et al. Perinatal and early postnatal changes in the expression of monocarboxylate transporters MCT1 and MCT2 in the rat forebrain. J Comp Neurol 2003;465:445–54.

[21] Polet F, Feron O. Endothelial cell metabolism and tumour angiogenesis: glucose and glutamine as essential fuels and lactate as the driving force. J Intern Med 2013;273:156–65.

[22] Speder P, Liu J, Brand AH. Nutrient control of neural stem cells. Curr Opin Cell Biol 2011;23:724–9.

[23] Alvarez Z, Mateos-Timoneda MA, Hyrossova P, Castano O, Planell JA, Perales JC, et al. The effect of the composition of PLA films and lactate release on glial and neuronal maturation and the maintenance of the neuronal progenitor niche. Biomaterials 2013;34:2221–33.

[24] Mattotti M, Alvarez Z, Ortega JA, Planell JA, Engel E, Alcantara S. Inducing functional radial glia-like progenitors from cortical astrocyte cultures using micropatterned PMMA. Biomaterials 2012;33:1759–70.

[25] Li Y, Song Y, Zhao L, Gaidosh G, Laties AM, Wen R. Direct labeling and visualization of blood vessels with lipophilic carbocyanine dye DiI. Nat Protoc 2008;3:1703–8.

[26] Conte WL, Kamishina H, Reep RL. Multiple neuroanatomical tract-tracing using fluorescent Alexa Fluor conjugates of cholera toxin subunit B in rats. Nat Protoc 2009;4:1157–66.

[27] Fan HJ, Knez M, Scholz R, Hesse D, Nielsch K, Zacharias M, et al. Influence of surface diffusion on the formation of hollow nanostructures induced by the Kirkendall effect: the basic concept. Nano Lett 2007;7:993–7.

[28] Feng L, Hatten ME, Heintz N. Brain lipid-binding protein (BLBP): a novel signaling system in the developing mammalian CNS. Neuron 1994;12:895–908.

[29] Englund C, Fink A, Lau C, Pham D, Daza RA, Bulfone A, et al. Pax6, Tbr2, and Tbr1 are expressed sequentially by radial glia, intermediate progenitor cells, and postmitotic neurons in developing neocortex. J Neurosci 2005;25:247–51.

[30] Suh H, Consiglio A, Ray J, Sawai T, D'Amour KA, Gage FH. In vivo fate analysis reveals the multipotent and self-renewal capacities of Sox2+ neural stem cells in the adult hippocampus. Cell Stem Cell 2007;1:515–28.

[31] Hsieh J. Orchestrating transcriptional control of adult neurogenesis. Genes Dev 2012;26:1010–21.

[32] Ovens MJ, Davies AJ, Wilson MC, Murray CM, Halestrap AP. AR-C155858 is a potent inhibitor of monocarboxylate transporters MCT1 and MCT2 that binds to an intracellular site involving transmembrane helices 7–10. Biochem J 2010;425:523–30.

[33] Miller FD, Gauthier AS. Timing is everything: making neurons versus glia in the developing cortex. Neuron 2007;54:357–69.

[34] Tavazoie M, Van der Veken L, Silva-Vargas V, Louissaint M, Colonna L, Zaidi B, et al. A specialized vascular niche for adult neural stem cells. Cell Stem Cell 2008;3:279–88.

[35] Shechter R, Miller O, Yovel G, Rosenzweig N, London A, Ruckh J, et al. Recruitment of beneficial M2 macrophages to injured spinal cord is orchestrated by remote brain choroid plexus. Immunity 2013;38:555–69.

[36] Hisaoka T, Nakamura Y, Senba E, Morikawa Y. The forkhead transcription factors, Foxp1 and Foxp2, identify different subpopulations of projection neurons in the mouse cerebral cortex. Neuroscience 2010;166:551–63.

[37] Magavi SS, Leavitt BR, Macklis JD. Induction of neurogenesis in the neocortex of adult mice. Nature 2000;405:951–5.

[38] Fame RM, MacDonald JL, Macklis JD. Development, specification, and diversity of callosal projection neurons. Trends Neurosci 2011;34:41–50.

[39] Freire E, Gomes FC, Jotha-Mattos T, Neto VM, Silva Filho FC, Coelho-Sampaio T. Sialic acid residues on astrocytes regulate neuritogenesis by controlling the assembly of laminin matrices. J Cell Sci 2004;117:4067–76.

[40] Lathia JD, Rao MS, Mattson MP, Ffrench-Constant C. The microenvironment of the embryonic neural stem cell: lessons from adult niches? Dev Dyn 2007;236:3267–82.

[41] Hurtado A, Cregg JM, Wang HB, Wendell DF, Oudega M, Gilbert RJ, et al. Robust CNS regeneration after complete spinal cord transection using aligned poly-ʟ-lactic acid microfibers. Biomaterials 2011;32:6068–79.

[42] Ma S, Kwon HJ, Johng H, Zang K, Huang Z. Radial glial neural progenitors regulate nascent brain vascular network stabilization via inhibition of Wnt signaling. PLoS Biol 2013;11:e1001469.

[43] Simon-Assmann P, Orend G, Mammadova-Bach E, Spenle C, Lefebvre O. Role of laminins in physiological and pathological angiogenesis. Int J Dev Biol 2011;55:455–65.

[44] Kazanis I, Lathia JD, Vadakkan TJ, Raborn E, Wan R, Mughal MR, et al. Quiescence and activation of stem and precursor cell populations in the subependymal zone of the mammalian brain are associated with distinct cellular and extracellular matrix signals. J Neurosci 2010;30:9771–81.

[45] Belvindrah R, Graus-Porta D, Goebbels S, Nave KA, Muller U. Beta1 integrins in radial glia but not in migrating neurons are essential for the formation of cell layers in the cerebral cortex. J Neurosci 2007;27:13854–65.

[46] Loulier K, Lathia JD, Marthiens V, Relucio J, Mughal MR, Tang SC, et al. beta1 integrin maintains integrity of the embryonic neocortical stem cell niche. PLoS Biol 2009;7:e1000176.

[47] Benner EJ, Luciano D, Jo R, Abdi K, Paez-Gonzalez P, Sheng H, et al. Protective astrogenesis from the SVZ niche after injury is controlled by Notch modulator Thbs4. Nature 2013;497:369–73.

[48] Saha B, Peron S, Murray K, Jaber M, Gaillard A. Cortical lesion stimulates adult subventricular zone neural progenitor cell proliferation and migration to the site of injury. Stem Cell Res 2013;11:965–77.

[49] Niu W, Zang T, Zou Y, Fang S, Smith DK, Bachoo R, et al. In vivo reprogramming of astrocytes to neuroblasts in the adult brain. Nat Cell Biol 2013;15:1164–75.

[50] Christensen K, Schroder HD, Kristensen BW. CD133 identifies perivascular niches in grade II–IV astrocytomas. J Neurooncol 2008;90:157–70.